Mathematical modeling of CO 2 absorption with ionic liquids in a membrane contactor, study of absorption kinetics and influence of temperature

Sohaib Qazi, Lucía Gómez-coma, Jonathan Albo, Stéphanie Druon-bocquet, Angel Irabien, Mohammad Younas, José Sanchez-Marcano

Mathematical Modelling of CO_2 Absorption with Ionic Liquids in a Membrane Contactor, Study of Absorption Kinetics and Influence of Temperature

Sohaib Qazi[1], Lucía Gómez-Coma[2], Jonathan Albo[2], Stéphanie Druon-Bocquet[1], Angel Irabien[2], Mohammad Younas[3], José Sanchez-Marcano[1]

1: Institut Européen des Membranes, IEM – UMR 5635, CNRS, ENSCM, Université de Montpellier, Montpellier, France.

2: Chemical and Biomolecular Engineering Department, Universidad de Cantabria, Av. Los Castros, 39005 Santander, Spain.

3: Department of Chemical Engineering, University of Engineering and Technology, Peshawar, P.O. Box 814, University Campus, Peshawar 25120, Pakistan

Abstract

BACKGROUND: This work presents a comprehensive study of CO_2 capture from CO_2/N_2 mixtures in a hollow fiber membrane contactor (HFMC). The absorbents considered were three different ionic liquids (ILs): 1-Ethyl-3-methylimidazolium acetate ([emim][OAc]), 1-ethyl-3-methylimidazolium ethylsulfate ([emim][$EtSO_4$]) and 1-ethyl-3-methylimidazolium methyl sulfate ([emim][$MeSO_4$]). A comprehensive 2-D mathematical model for the transport of CO_2 was developed and solved for steady-state and pseudo steady-state modes. For pseudo steady-state mode, the 2-D model was linked with a dynamic model applied on a tank from which IL was recirculated into the shell side of the HFMC.

RESULTS: The model showed excellent agreement between the simulations and experimental data within the range of 2-5 % standard deviation. Initially, overall mass transfer coefficients of 7.6×10^{-6} ($m.s^{-1}$), 1.6×10^{-6} ($m.s^{-1}$) and 3.7×10^{-6} ($m.s^{-1}$) were obtained for [emim][OAc], [emim][$EtSO_4$] and [emim][$MeSO_4$], respectively. Solubility, diffusivity and absorption efficiency of CO_2 in ILs showed strong dependence on the temperature. Furthermore, concentration drop in the wetted portion of the membrane, effect of porosity, tortuosity, gas and absorbent flow rates were systematically studied.

CONCLUSION: Findings of both experimental and modelling work suggests that in spite of the difference of extraction efficiency, these ILs are potential absorbents for CO_2 in membrane contactors. Moreover, the modelling approach was found very effective to predict the absorption behavior of CO_2 in ILs and to study the wetting phenomena and parametric effects.

Keywords: CO_2 Absorption, CO_2 solubility, Membrane Contactor, Ionic Liquid, Modelling and Simulation.

Nomenclature

A	Area (m^2)
C	Concentration $(mol.m^{-3})$
D	Diffusivity $(m^2.s^{-1})$
E	Activation energy $(KJ.mol^{-1})$
f	Fugacity (Pa)
H	Henry's law constant (Pa)
$\Delta\hat{H}$	Enthalpy $(KJ.mol^{-1})$
j	Molar flux $(mol.m^{-2}.s^{-1})$
K	Equilibrium constant (-)
Ḱ	Mass transfer coefficient $(m.s^{-1})$
L	Length of membrane(m)
$\acute{m}$	Distribution factor of CO_2 (-)
M	Molar weight $(kg.mol^{-1})$
n	Number of fibers
P	Pressure (Pa)
Q	Volumetric flowrate $(m^3.s^{-1})$
r	Radial coordinate (m)
r_1	Inner radius of the tube (m)
r_2	Outer radius of the tube (m)
r_3	Radius of the free surface (m)
R	Module inner radius(m)
Ŕ	Reaction rate $(mol.m^{-3}.s^{-1})$
$\Re_g$	Perfect gas constant $(j.mol^{-1}.K^{-1})$
t	Time(s)
T	Temperature (K)
u	Average velocity $(m.s^{-1})$
U	Velocity $(m.s^{-1})$
v	Molar volume $(cm^3.mol^{-1})$
V	Volume (m^3)
x	Mole fraction of CO_2 in IL (-)
z	Axial coordinate(m)

Subscripts

CO_2	Carbon dioxide
eq	Equilibrium
$\boldsymbol{g}$	Gas
$\boldsymbol{i}$	Component i
$\boldsymbol{IL}$	Ionic Liquid
in	Inlet
$\boldsymbol{l}$	Liquid
N_2	Dinitrogen
out	Outlet
ov	Overall
r	Radial
Z	Axial

Greek Letters

μ	Viscosity (cP)
Θ	Contactor volumetric void fraction (-)
ρ	Density $(kg.m^{-3})$
$\bar{\upsilon}$	Atomic diffusion volume (unity)
ε	Membrane porosity (-)
τ	Membrane tortuosity (-)
$\mathcal{T}$	Ionic liquid residence time (s)
δ	Membrane thickness (m)
φ_{v}	CO_2 amount in feed gas (% vol)
θ	Cylindrical coordinate (rad)
Ø	Fugacity coefficient (-)

1 Introduction

Increased emissions of carbon dioxide (CO_2), a major greenhouse gas and climate change contributor, is a serious concern all over the world [1–3]. According to the International Panel of Climate Change (IPCC) for year 2100 it is estimated that the CO_2 content in the atmosphere will reach 570 ppmv and the mean temperature will rise by 2^oC [3–5]. Scientists and technologists are significantly focusing on carbon capture (CC), which is a promising route to reduce CO_2 emissions. Pre-combustion and post-combustion (PC) technologies for CC have been extensively studied in recent years and presented as economical and efficient techniques to mitigate CO_2 emissions. Among CC technologies, PC is a promising technique as it can be retrofitted to existing power plants [6–9].

Numerous technologies are used for CC based on both physical and chemical process involving absorption, adsorption, membrane separation, conversion and cryogenic separation [10,11]. Membrane gas absorption (MGA) process integrates conventional gas-liquid absorption with membrane contactors as a base for mass transfer. Membrane contactors have a promising intensification potential with major advantages such as high specific surface area, independent gas-liquid flow rates, flexibility and modularity, while gas absorption leads to high selectivity and high driving force [12–18]. Various physical and chemical absorbents have been used for CC in membrane contactors. An absorbent is rated based on its selectivity for gas, good solubility, good reactivity, and high absorption, low energy consumption during regeneration, low volatility and high contact angle with the membrane [19,20]. Monoethanolamines [21,22], diethanol amines [22,23], methyldiethanolamine [21–23], 2-amino-2-methyl-1-propanol [22] and other absorbents [24,25] have been used for CC with membrane contactors in previous studies. Alternative absorption fluids namely ionic liquids (ILs) have been proposed to replace corrosive and volatile amine based solvents [26–28].

ILs have been paid much attention in recent years and regarded as potential candidates for CO_2 absorption. An IL is a salt, which consist exclusively of organic cations and inorganic or organic anions, with a melting point lower than 100 ^oC [26]. ILs are divided in two sub categories, room temperature ILs (RTILs) and task specific ILs (TSILs) [8]. RTILs are conventional ILs which behaves like typical physical absorbents for the solubility of gases. Solubility of gases in RTILs is mostly represented by Henry's Law constant. TSILs are able to absorb more CO_2 compared to RTILs, due to both physical and chemical absorption. However, the regeneration of TSILs is very energy consuming and costly due to chemical bonding. Properties like high CO_2 solubility, negligible volatility, high thermal stability, non-flammability, tunability and potential for replacing conventional absorbents are the major driving forces for research on ILs [26,29–32]. Many review studies on CO_2 absorption with ILs have been reported in recent years. These studies have listed absorption capacities and parameters for a number of ILs with both physical and chemical absorption nature for CO_2 [8,26,30,33,34]. Other studies have focused on investigating pressure-temperature-composition data for CO_2 absorption in various ILs followed by analysis of the data using an equation-of-state (EOS) model [35–38].

Recently, many studies have been devoted to membrane absorption with membrane contactors using ILs as absorbent. IL [emim][$EtSO_4$] which is reported to behave as a physical absorbent for CO_2, has been used in many studies. This ionic liquid was used for both SO_2 and CO_2 capture in cross-flow membrane contactors [39,40]. This research group systematically performed the comparative analysis of CO_2 capture in

parallel-flow and cross-flow membrane contactors [41]. ILs 1-butyl-3-methyl-imidazolium tetrafluoroborate [bmim][BF_4] and 1-(3- aminopropyl)-3-methyl-imidazolium tetrafluoroborate [apmim][BF_4] have also been used with membrane contactors to study CO_2 absorption and desorption. Chemical absorption with [apmim][BF_4] showed very high absorption capacity but low regeneration even at high vacuum degrees [12]. Influence of temperature on physical and chemical absorption of CO_2 with [emim][$EtSO_4$] and [emim][OAc] was studied by Gómez-Coma et al[42]. Jie et al[43] and Chau et al[44] used 1-butyl-3-methylimidazolium dicyanamide [bmim][DCA] in a pressure swing membrane absorption process for CO_2 capture in membrane contactors.

Many studies on modelling of CO_2 absorption in membrane contactors have been published previously. However, up to the authors knowledge there is no study available on two dimensional (2-D) dynamic modelling of both physical and chemical absorption of CO_2 in ILs, with an effective study of the temperature influence. 2-D model is an approach allowing calculating both axial and radial mass transfers. Then the model is applicable to real absorption situations. It also allows to evaluate the role of absorbent, membrane and hydrodynamics separately as it has been suggested in the review of Zhao et al[9]. In the present study, a comprehensive 2-D mass transfer model was developed for CO_2 absorption (chemical & physical) in membrane contactors with three different ILs (same cation and different anions) namely, 1-Ethyl-3-methylimidazolium acetate ([emim][OAc]), 1-ethyl-3-methylimidazolium ethylsulfate ([emim][$EtSO_4$]) and 1-ethyl-3-methylimidazolium methyl sulfate ([emim][$MeSO_4$]). Both, [emim][OAc] and [emim][$EtSO_4$] are efficient absorbents for CO_2 having low values of Henry constant high values of viscosities and considerable values of surface tension to avoid wetting of membrane pores. [emim][$MeSO_4$] is a potential absorbent for CO_2, based on the solubility data and Henry's law constants reported by Yim et al.[36], Mejía et al.[34] and Finotello et al.[45] in their studies. This IL has not been considered until now for CO_2 absorption on membrane contactors. Moreover, [emim][$MeSO_4$] is a viscous IL with a very high value of surface tension among other ILs. These properties make it a potential candidate for using it with hydrophobic membranes to avoid membrane wetting. Structures of the considered ILs are presented in Figure 1.

Figure 1

Counter current gas-IL arrangements were adopted for the model. Detailed concentration profiles (both axial and radial) for all three IL were developed. Evolution of overall mas transfer coefficient (K_{ov}) with recirculation time of absorbents was studied. Effects of temperature on diffusivity (ILs and gas phase) and Henry constant of the three ILs were investigated. These parameters were further linked with the model in order to investigate temperature effects on the absorption behavior of CO_2 with the ILs.

2 Model development

A comprehensive 2-D model is presented here for CO_2 mass transport in a hollow fiber membrane contactor for both steady-state and pseudo steady-state modes. The process is explained in Figure 2. The dotted lines show steady-state mode in which both gas and IL are passed from the membrane contactor in a non-closed loop. In the pseudo steady-state mode IL is recirculated from a reservoir which is represented by solid lines while gas flows in a non-closed loop. Fresh CO_2/N_2 gaseous mixture is

introduced into the inner side of hollow fibers. While IL flows in the shell side either in a closed loop or non-closed loop. For pseudo steady-state mode, a dynamic model is linked with the mass transport model for the recirculated IL in the tank.

Figure 2

A polypropylene membrane contactor module with the same properties than Liquicel™ membrane contactors (USA) with macro-mesoporous, thin walled, opaque, polypropylene hollow-fibers was considered for the separation of CO_2 from CO_2/N_2 mixture using ILs. Characteristics of the module and operating conditions are presented in Table 1. Properties of the three ILs studied here, are presented in Table 2. As described in the introduction, [emim][OAc] and [emim][$EtSO_4$] are efficient absorbents for CO_2 having high value of viscosity and considerable value of surface tension to avoid wetting membrane pores. [emim][$MeSO_4$] is the less viscous IL but presents the highest value of surface tension among ILs studied. These properties make it also a potential candidate for using it in membrane contactors. In order to reach reasonable computing times, we considered for the model establishment a single hollow fiber with arbitrary shell predicted by Happel's model[46]. A portion of the fiber along with the arbitrary shell (Figure 3) was modeled. Continuity equations were solved for the three domains of the flow cell namely, tube, membrane and shell.

Table 1

Table 2

Figure 3

The mass transport model of the flow cell (Figure 3) is based on the following assumptions:

a) Countercurrent mode for gas and IL flow in membrane contactor
b) Fully developed velocity profile in the shell and tube
c) Steady-state and isothermal conditions inside HFMC module (unless mentioned)
d) Laminar flow conditions
e) Application of Henry's law on gas-liquid interface
f) Non-selective behavior of the membrane
g) Perfectly stirred absorbent tank

2.1 Mass transfer equations

A schematic diagram of the countercurrent flow of gas and IL is shown in Figure 3. Mass balances were carried out for each of the three domains shown in Figure 3. The continuity equation for each section is expressed as:

$$\frac{\partial C_i}{\partial t} = -\nabla . C_i U - \nabla . j_i + \acute{\mathrm{R}}_i \quad (1)$$

Where the concentration of the species is $\mathrm{C_i}(\mathrm{mol.\,m^{-3}})$, $\mathrm{U}\ (\mathrm{ms^{-1}})$ is the velocity, $\mathrm{j_i}\ (\mathrm{mol.\,m^{-2}.\,s^{-1}})$ is the molar flux, $\acute{\mathrm{R}}_\mathrm{i}\ (\mathrm{mol.\,m^{-3}.\,s^{-1}})$ is the reaction rate and $\mathrm{t}\ (\mathrm{s})$ is the time. The steady-state form of the equation is presented below:

$$0 = -\nabla . C_i U - \nabla . j_i + \acute{R}_i \quad (2)$$

Terms on the right-hand side of the equation represents convection, diffusion and reaction. Fick's law of diffusion is applicable for the diffusion in membrane contactor [47].

2.1.1 Lumen side of the membrane contactor

Transport of gas in the inner (tube) side is due to axial radial diffusion and axial convection. Equation 1 can be rewritten for the tube side as below.

$$\frac{\partial C_{CO_2-tube}}{\partial t} + D_{CO_2-tube}\left[\frac{\partial^2 C_{CO_2-tube}}{\partial r^2} + \frac{1}{r}\frac{\partial C_{CO_2-tube}}{\partial r} + \frac{\partial^2 C_{CO_2-tube}}{\partial z^2}\right] = U_{z-tube}\frac{\partial C_{CO_2-tube}}{\partial z} \quad (3)$$

Equation can be expressed in steady-state as below.

$$D_{CO_2-tube}\left[\frac{\partial^2 C_{CO_2-tube}}{\partial r^2} + \frac{1}{r}\frac{\partial C_{CO_2-tube}}{\partial r} + \frac{\partial^2 C_{CO_2-tube}}{\partial z^2}\right] = U_{z-tube}\frac{\partial C_{CO_2-tube}}{\partial z} \quad (4)$$

CO_2 gas phase diffusivity in equation 3 and 4 can be estimated by the following expression [48]:

$$D_{CO_2-tube} = \frac{0.01013.T^{1.75}\left(\frac{1}{M_{CO_2}}+\frac{1}{M_{N_2}}\right)^{0,5}}{P*\left[\left(\sum \bar{\upsilon}_{CO_2}\right)^{\frac{1}{3}}+\left(\sum \bar{\upsilon}_{N_2}\right)^{\frac{1}{3}}\right]^2} \quad (5)$$

In the above equation $\bar{\upsilon}$ is the atomic diffusion volume. The validation of the correlation has been verified by many authors in previous studies [49–51].

As the velocity profile inside the tube is laminar, the velocity distribution can be expressed by equation (6).

$$U_{z-tube} = 2u_{tube}\left[1 - \left(\frac{r}{r_1}\right)^2\right] \quad (6)$$

Where u_{tube} $(m.s^{-1})$ in equation 6 represents average velocity of the gas in the tube.

Boundary conditions are listed in table 3.

2.1.2 Porous membrane

Axial and radial diffusion are considered for mass transfer in membrane. Then, equation 1 can be rewritten for the membrane as below:

$$\frac{\partial C_{CO_2-tube}}{\partial t} + D_{CO_2-membrane}\left[\frac{\partial^2 C_{CO_2-membrane}}{\partial r^2} + \frac{1}{r}\frac{\partial C_{CO_2-membrane}}{\partial r} + \frac{\partial^2 C_{CO_2-membrane}}{\partial z^2}\right] = 0 \quad (7)$$

For steady-state mode the equation can be expressed as below.

$$D_{CO_2-membrane}\left[\frac{\partial^2 C_{CO_2-membrane}}{\partial r^2} + \frac{1}{r}\frac{\partial C_{CO_2-membrane}}{\partial r} + \frac{\partial^2 C_{CO_2-membrane}}{\partial z^2}\right] = 0 \quad (8)$$

Effective diffusivity inside the porous membrane is expressed as:

$$D_{CO_2-membrane} = D_{CO_2-tube}\,\frac{\varepsilon}{\tau} \quad (9)$$

Where ε and τ represents porosity and tortuosity of the porous membrane.

Boundary conditions are listed in table 3.

2.1.3 Shell side of the membrane contactor

ILs flow counter currently through the shell side of the contactor. IL [emim][OAc] is found to behave as both physical and chemical absorbent for CO_2 [35,37] while both [emim][$EtSO_4$] and [emim][$MeSO_4$] behave as physical absorbent for CO_2 [36,52,53].

CO_2 solubility in ILs is mostly represented by Henry's law constant. Moreover, generally the models consider Henry's law for the gas liquid interface. Indeed, the calculations of this constant are of high importance for the modeling of CO_2 absorption on ILs. The magnitude of the Henry's constant indicates whether the absorption is chemical or physical. A small value of Henry's constant (usually less than 3 MPa) denotes chemical absorption of CO_2 in ILs [35,54] and high gas solubility [28,55]. In this work the experimental PTx data (vapour-liquid equilibria: VLE) were obtained from the literature for the three ILs [emim][OAc] [36], [emim][$EtSO_4$] [52,53], [emim][$MeSO_4$] [36]. Henry's constants were calculated from these experimental PTx data using the following equation [35,56–58] :

$$H(T,P) = \lim_{x\to 0} \frac{f(T,P,x_{CO_2})}{x_{CO_2}} = \lim_{x\to 0} \frac{\emptyset(T_{eq},P_{eq})\,P_{eq}}{x_{CO_2}} \quad (10)$$

Where $H(Pa)$ is the Henry's constant, f is the fugacity of CO_2, x_{CO_2} is the mole fraction of CO_2 dissolved in IL, $\emptyset$ is the fugacity coefficient, T_{eq} is the equilibrium temperature and $P_{eq}$is the equilibrium pressure. As the solubility varies with temperature, equation 10 allowed calculating Henry's constant at various temperatures. As described in the introduction, the three ILs studied are efficient absorbents for CO_2 having low values of Henry constant. Values of this constant, for the three ILs, at 298 K are listed in table 4. The constant found from equation 10 was used in the following equation to calculate dimensionless Henry's constant [58]:

$$\acute{m} = \frac{\rho_{IL}\,\mathcal{R}_g\,T}{M_{IL}\,H} \quad (11)$$

Where $\rho_{IL}(kg.m^{-3})$ is the density of IL, $\mathcal{R}_g(m^3.Pa.K^{-1}.mol^{-1})$ is the gas constant, M_{IL} $(kg.mol^{-1})$ is the molar weight of IL, T (K) is the temperature and $H(Pa)$ Henry's law constant for CO_2 in the three ILs. For the three ILs, [emim][OAc], [emim][$EtSO_4$], [emim][$MeSO_4$], densities had strong dependency on temperature which in turn affected the Henry's constant and solubility of CO_2. Temperature dependency of the density for the three ILs [emim][OAc], [emim][$EtSO_4$], [emim][$MeSO_4$] are shown in equations 12, 13, and 14, respectively [52,59–62]. Equations below correspond to density in $kg.m^{-3}$ and temperature in K:

$$\rho(T) = 1280.8 + 0.608\,T \quad (12)$$

$$\rho(T) = 1451.5928 - 0.757562\,T + 0.00013391\,T^2 \quad (13)$$

$$\ln\rho(T) = 7.33100 - 6.17220 \times 10^{-4}\,T + 1.3862 \times 10^{-4}\,T^2 \quad (14)$$

The reaction term of equation 6 is neglected for all three ILs. Experimental solubility data from the literature at VLE is used to measure the Henry's constant and partition coefficient for CO_2 solubility in ILs. The experimental solubility data covers both physical and chemical absorption. The partition coefficient (equation 2) measured from the experimental VLE solubility data of CO_2 was used to define the concentration distribution across the gas-liquid interface which resides on/or between the two boundaries of porous membrane depending upon the conditions whether the membrane is wetted or non-wetted (figure 3). Values of Henry's constant are presented in table 4. Gómez-Coma et al.[63] transformed the value of overall mass transfer coefficient for [emim][OAc] to a reaction constant. The transformed constant agrees with the first order gas liquid chemical reaction:

$$K_r = K_{ov} \frac{Fiber\ Area}{Shell\ Volume} \tag{15}$$

Furthermore, the activation energy was calculated using Arrhenius equation:

$$K_r = Be^{\frac{-E_a}{RT}} \tag{16}$$

Where B is the pre-exponential factor, E_a is the activation energy($J.mol^{-1}$), R is the gas constant $8.31\ J.K^{-1}mol^{-1}$, and T is the temperature (K). These values are presented in table 4 along with the equilibrium constant and enthalpy of complex formation [35,38].

Transport of CO_2 in the shell side is due to axial radial diffusion and axial convection. Based on the above assumptions, equation 1 can be rewritten for the shell side as below:

$$\frac{\partial C_{CO_2-tube}}{\partial t} + D_{CO_2-shell}\left[\frac{\partial^2 C_{CO_2-shell}}{\partial r^2} + \frac{1}{r}\frac{\partial C_{CO_2-shell}}{\partial r} + \frac{\partial^2 C_{CO_2-shell}}{\partial z^2}\right] = U_{z-shell}\frac{\partial C_{CO_2-shell}}{\partial z} \tag{17}$$

For steady-state mode equation 17 can be rewritten as follows:

$$D_{CO_2-shell}\left[\frac{\partial^2 C_{CO_2-shell}}{\partial r^2} + \frac{1}{r}\frac{\partial C_{CO_2-shell}}{\partial r} + \frac{\partial^2 C_{CO_2-shell}}{\partial z^2}\right] = U_{z-shell}\frac{\partial C_{CO_2-shell}}{\partial z} \tag{18}$$

$D_{CO_2-shell}$ can be expressed as [64]:

$$D_{CO_2-shell} = 2.66 \times 10^{-3}\frac{1}{\mu_{IL}^{0.66} v_{CO_2}^{1.04}} \tag{19}$$

Where $\mu_{IL}(mPa.s)$ and $v_{CO_2}(cm^3.mol^{-1})$ are viscosity of IL and molar volume of CO_2. Temperature dependency of the viscosity for the three ILs [emim][OAc], [emim][$EtSO_4$], [emim][$MeSO_4$] are presented in equations below, respectively[52,59–62]. Equations below correspond to viscosity in $(mPa.s)$ and temperature in K:

$$\ln \mu(T) = -1.657 + \left(\frac{673.7}{T-196.1}\right) \tag{20}$$

$$\ln \mu(T) = -1.6558 + \left(\frac{792.98}{T-171.15}\right) \tag{21}$$

$$\ln \mu(T) = \ln \rho M - 18.25 + \left(\frac{1266.1}{T}\right) \tag{22}$$

Equation 19 developed by Morgan et al. [64] is based on the CO_2 diffusivities in imidazolium cation based ILs with different anions. Many authors have confirmed this correlation by comparing experimental diffusivities with the diffusivities measured by this correlation [56,65]. Calculated values of CO_2 diffusivity, for the three ILs, at 293 K are listed in table 4.

Velocity profile inside the shell is expressed by Happel's free surface model [46].

$$U_{z-shell} = 2u_{shell}\left[1-(\frac{r_2}{r_3})^2\right]\frac{(r/r_3)^2-(r_2/r_3)^2+2\ln(r_2/r)}{3+(r_2/r_3)^4-4(r_2/r_3)^2+4ln(r_2/r_3)} \quad (23)$$

Where u_{shell}, r_2 and r_3 are average velocity of absorbent in the shell, outer radius of fiber and radius of free surface. The relationship between r_2 and r_3 is expressed as:

$$r_3 = \left(\frac{1}{1-\Theta}\right)^{1/2} r_2 \quad (24)$$

Where Θ is the volume fraction of the void space, which can be calculated from the following equation:

$$1-\Theta = \frac{nr_2^2}{R^2} \quad (25)$$

Where n is the number of fibers and R is the module inner radius.

Boundary conditions are listed in Table 3.

Table 3

Table 4

2.1.4 Dynamic model: Pseudo steady-state

As it has been explained in the preceding sections, in the pseudo steady-state mode IL passing through the shell side of the membrane contactor is recirculated from the tank as shown in Figure 2. CO_2 concentration gradually increases in the IL phase with the number of circulation-paths in the membrane contactor setup. The CO_2 concentration evolution with time was calculated by applying a transient differential equation around the tank:

$$Q_{IL}\left(C_{CO_2-Z=0}(t) - C_{CO_2-tank}(t)\right) = V_{IL}\frac{dC_{CO_2-tank(t)}}{dt} \quad (26)$$

Where $C_{CO_2-tank}(t)$ is CO_2 concentration $(mol.m^{-3})$ in tank at time t, $C_{CO_2-Z=0}(t)$ is shell side concentration $(mol.m^{-3})$ of CO_2 at z=0 which is the exit of the contactor to the absorbent tank, V_{IL} (m^3) and $Q_{IL}(m^3.s^{-1})$ are the total volume and the volumetric flow rate of ionic liquid. Solving equation (26) for the CO_2 concentration in the tank at time $t+\Delta t$ gives the following expression:

$$C_{CO_2-tank}(t+\Delta t) = \frac{\Delta t}{\mathcal{T}_{IL}}\ C_{CO_2-Z=0}(t) + C_{CO_2-tank}(t)\left[1+\frac{\Delta t}{\mathcal{T}_{IL}}\right] \quad (27)$$

where $\mathcal{T}_{IL} = \frac{V_{IL}}{Q_{IL}}$ is the residence time of IL in the tank.

$C_{CO_2-Z=0}(t)$ was found using the following boundary integration equation:

$$C_{CO_2-Z=0}(t) = \frac{\int\int_{r=r_2}^{r=r_3} C_{CO_2-shell}(r) r dr d\theta}{\int\int_{r=r_2}^{r=r_3} r dr d\theta} \quad (28)$$

2.1.5 Model simulation and numerical approach

The set of equations for tube, membrane and shell side presented in the preceding sections were coupled and solved using COMSOL Multiphysics® (version 5.3a, 2018) and MATLAB R2017a using LiveLink™ for MATLAB®. The model equations were solved using PARDISO solver, which is a high performance, robust and memory efficient solver for solving large sparse symmetric and non-symmetric linear system of equations. The finite element method was used to solve partial differential equations. Mapped meshing was applied with 4 different distributions for different boundaries. For pseudo steady-state study, a time dependent solver was applied while keeping the same mapping and solver configurations. The time dependent solver was set for BDF (backward differentiation formula) time stepping, with strict steps for the solver. BDF is an implicit solver that uses backward differentiation formulas with variation from 1-5 in order of accuracy. BDF methods are known for their higher stability and provides variable orders. A higher order is used when needed and a lower order is automatically employed when it is required for stability. The process was fully coupled.

As for pseudo steady-state mode the concentration is constantly evolving with time. The evolution of CO_2 concentration with recirculation of IL was measured by equation (27). Dynamic equation was coupled with the mass transfer equations. $C_{CO_2-Z=0}(t)$ term for the dynamic model was defined from the boundary integral equation (28) after solving the mass transfer equations in COMSOL. The code for the dynamic model predicts the change in concentration of CO_2 in the IL tank for the time $t + \Delta t$. Equation 27 defines input concentration of the absorbent side which for the steady-state is always zero (fresh solvent).

3 Results and discussion

3.1 Pseudo steady-state mode

3.1.1 Model validation: Comparison of simulation data with experimental results

Modelling results were compared with experimental data available from Gómez-Coma et al.[42] who used a polypropylene HFMC supplied by Liquicel™-Membrane Contactors (USA) (Table 1) in their study. Non-wetting conditions were assumed due to the fact of applying a slight transmembrane pressure difference. Considered ILs are highly viscous and have high values of surface tension (Table 2), making very feasible conditions for non-wetting of membrane.

For the model validation, we compared the calculated dimensionless concentration of CO_2 at the outlet of the tube (gas phase) against time with the experimental results for the three ILs [42]. ILs flow rate was kept at 50 ml.min^{-1} while gas flow rate was kept at 70 ml.min^{-1}. The CO_2 composition in the gas was 15 % by volume. Figure 4 (a) shows the results obtained for physical and chemical absorption of CO_2 with [emim][OAc] at two different temperatures. A gradual increase in outlet concentration of CO_2 can be

observed. It is evident from the results that the proposed model reproduces the experimental data reasonably. Figure 4 (b) presents the similar results for physical absorption of CO_2 with [emim][$EtSO_4$] and [emim][$MeSO_4$]. It can be seen that the simulation results for [emim][$EtSO_4$] are in good agreement with the corresponding experimental results. In this work, another IL [emim][$MeSO_4$] (having no experimental data available in the literature for CO_2 absorption with [emim][$MeSO_4$] using membrane contactors) with different absorption kinetics, was also studied. The ILs [emim][$MeSO_4$] and [emim][$EtSO_4$] have the same [emim] cation and are reported to behave as physical absorbents for CO_2 with some slight differences in the physical constants. It has been reported that the solubility of CO_2 in the IL increases with the alkyl chain of the imidazolium cation. However, the effect of alkyl chain cations on the solubility of CO_2 is very less compared to anions. CO_2 molecules show greater affinity for the anions[30]. Performance of the membrane contactor gas absorption system is not only dependent on the solubility. Viscosity (affects diffusivity and flow of absorbent) and surface tension (affects wetting of the porous membrane) have also a strong influence on the performance. Indeed, as an initial approach the experimental values of CO_2 absorption with [emim][$EtSO_4$] in a HFMC were used for the validation of the model when [emim][$MeSO_4$] is considered as extracting fluid. IL [emim][$MeSO_4$] showed the same evolution of outlet concentration with recirculation time.

The results showed that even if the shape of the evolution is correct with time, the model always underestimates the experimental results. However, if experimental errors are considered, the standard deviations between the calculated and experimental results are ranged only between 2% to 5%.

Figure 4

3.1.2 Axial concentration distribution

The simulations of the 2-D axial concentration profile of CO_2 in the tube are presented in Figure 5. The gas mixture was introduced in the tube side at z=0. Moving toward z=L causes a gradual decrease in CO_2 concentration as it is absorbed progressively. Mass transfer in radial direction is mostly affected by diffusion while convection is the dominant mechanism for axial mass transfer due to gas flow. Figure 5(a) shows concentration profile of CO_2 with IL [emim][OAc] at t=1 min and t=100 min. This figure shows that very small contactor length is required to capture the whole amount of CO_2, initially, which verifies the presence of a very strong driving force. It is evident that even after 100 minutes of recirculation [emim][OAc] is still able to capture CO_2. Concentration distribution of CO_2 with IL [emim][$EtSO_4$] is presented in Figure 5(b). This figure shows that initially [emim][$EtSO_4$] is able to capture the whole amount of CO_2 but unlike [emim][OAc], even after 40 minutes the IL is almost unable to capture more CO_2. Moreover, compared to [emim][OAc] a larger contactor length is required. [emim][OAc] was more efficient because of the lower Henry's constant and higher CO_2 absorption ratio at VLE. IL [emim][$MeSO_4$] as a physical absorbent is more efficient compared to [emim][$EtSO_4$] as it captures CO_2 with a smaller contactor length and is able to absorb more CO_2 after 40 minutes. The concentration distribution is shown in figure 5(c).

Figure 5

3.1.3 Overall mass transfer coefficient

The overall mass transfer coefficient (K_{ov}) was calculated from the gas side flux (N_{CO_2-g}) and concentration gradient through the membrane. Equations 29-31 were used to estimate K_{ov}.

$$N_{CO_2-g} = \frac{Q_{g-in}\, C_{CO_2-in} - Q_{g-out}\, C_{CO_2-out}}{A} = K_{ov}\, \Delta C_{g-lm} \quad (29)$$

Where Q_{g-in} and Q_{g-out} are gas side inlet and outlet flow rates($m^3.s^{-1}$), respectively, C_{CO_2-in} and C_{CO_2-out} are gas side inlet and outlet concentrations($mol.m^{-3}$) of CO_2, respectively, while A denotes the active area (m^2) of membrane. C_{CO_2-out} was found from the following boundary integral equation.

$$C_{CO_2-out} = \frac{\int \int_{r=0}^{r=r_1} C_{CO_2-tube}(r) r dr d\theta}{\int \int_{r=0}^{r=r_1} r dr d\theta} \quad (30)$$

ΔC_{g-lm} in equation (29) represents logarithmic mean of driving force based on gas phase concentration which can be calculated using equation 31.

$$\Delta C_{g-lm} = \frac{\left(C_{g-in} - C^*_{g-in}\right) - \left(C_{g-out} - C^*_{g-out}\right)}{\ln\left(\frac{C_{g-in} - C^*_{g-in}}{C_{g-out} - C^*_{g-out}}\right)} \quad (31)$$

Where C^*_{g-in} and C^*_{g-out} in equation 31 represents concentration of the gas phase in equilibrium with corresponding CO_2 concentration in the liquid phase C^*_l. Henry's Law constant ($C^*_g = H_d\, C^*_l$) is used to measure the equilibrium concentration of gas phase. The process was based on recirculation of IL in the shell side of the contactor. This resulted in variation of concentration gradient with time as the IL became more concentrated with CO_2. The drop-in concentration gradient directly affects the overall mass transfer coefficient. Figure 6 represents the variation of K_{ov} in the first 100 minutes of recirculation. Values of K_{ov} are much higher for [emim][OAc] than for [emim][$EtSO_4$] and [emim][$MeSO_4$]. Initially, the values of K_{ov} were very high, after they dropped rapidly in the first 20 minutes of recirculation. The drop became gradual and small for further recirculations. After 100 minutes, K_{ov} for [emim][OAc], [emim][$EtSO_4$] and [emim][$MeSO_4$] was recorded as 2.6 x 10^{-6} ($m.s^{-1}$), 0.14 x 10^{-6} ($m.s^{-1}$) and 0.065 x 10^{-6} ($m.s^{-1}$), respectively.

Figure 6

3.2 Steady-state mode

3.2.1 Transient state study

Steady-state conditions can be achieved by passing both gas and IL from the membrane contactor in a non-closed loop. To achieve steady-state conditions throughout the membrane contactor, it must pass from the transient state during which concentration changes with time, until reaching steady-state conditions. Equation 8, 12 and 17 were used to study the changes in concentration of CO_2 with time until reaching steady-state conditions. Figure 7 shows variation in concentration of CO_2 at a point inside the tube at the length of L/3. In the first minute of the absorption, the CO_2 concentration increases very fast as the gas mixture is introduced to the tube side of the contactor. A gradual increase can be seen after 1

minute of the absorption operation. The absorption process does not reach steady-state very quickly as there is a very small increment to CO_2 concentration with further passage of the absorption time. The absorption process can be considered steady-state after 2.5-3 minutes as the CO_2 concentration becomes uniform at this point inside the tube. After achieving steady-state inside the contactor, the setup can be further studied for effect of different parameters.

Figure 7

3.2.2 Solubility and diffusivity study: Effect of temperature

Unlike other conventional absorbents ILs can be used at high temperatures as their boiling points are close to or even higher than their decomposition temperatures [66]. The maximum temperature level kept for the current analysis was 353.15 K. This value is far lower from the decomposition temperatures of the three ILs ([emim][OAc] = 461 K [67], [emim][$EtSO_4$] = 628 K [68] and [emim][$MeSO_4$] = 635 K [68]). Temperature affects both solubility and diffusivity of CO_2 in ILs. Increase in temperature decreases viscosity which is a favorable feature for enhanced diffusivity. Figure 8 shows the effect of temperature on CO_2 diffusivity in the three ILs and gas mixture. Diffusivities were calculated using the correlations mentioned in the preceding sections, equation 5 for gas phase diffusivity and equation 19 for CO_2 diffusivity in ILs. Equation 19 developed by Morgan et al.[64] is based on CO_2 diffusivities in imidazolium cation based ILs with different anions. As explained previously, many authors have confirmed this correlation by comparing experimental diffusivities with the diffusivities measured by this correlation [56,65]. Temperature dependency of viscosity for the three ILs [emim][OAc], [emim][$EtSO_4$] and [emim][$MeSO_4$] have been studied by Nazet et al.[59]; Schmidt et al.[60] and Costa et al.[61], respectively. It is evident from the figure 8 that increase in temperature has effectively increased the diffusivity of CO_2 in ILs while the change in gas phase is almost negligible.

Figure 8

Solubility of CO_2 in ILs is related to Henry's law constant. Indeed, the solubility is negatively affected with increase in temperature [55,69]. The constant calculated using equation 1 was plotted against temperature and reported in figure 9. It was observed that increase in temperature for all three ILs has increased the constant which shows a decrease in solubility. Increasing temperature from 283.15 K to 353.15 K increases the constant by 4.2 MPa, 11.1 MPa and 15.1 MPa for the ILs [emim][OAc], [emim][$EtSO_4$] and [emim][$MeSO_4$], respectively.

Figure 9

Based on the above findings, temperature has two opposite effects on the absorption of CO_2 in room temperature ILs. Increase in temperature significantly reduces the viscosity of ILs, thus enhancing CO_2 diffusivity while CO_2 solubility in ILs decreases as Henry's law constant increases. To observe the overall effect of temperature on CO_2 absorption in ILs, radial concentration of CO_2 at tube side was evaluated by defining the same cut line of length r_1 for all three ILs. A single value of concentration was noted as due to high diffusivity at tube side there was a negligible variation in concentration along the radial length. Table 5 presents values of CO_2 concentration (radial) in the tube at different temperatures. Temperature has an evident effect on capture ratio as increasing the temperature has increased the concentration at the outlet. A huge difference in the concentration of CO_2 was noted for the three ILs at the same radial

length. From the results it can be concluded that despite the significant enhancement of CO_2 diffusivity with increase in temperature, the overall absorption decreases as the CO_2 solubility is negatively affected.

Table 5

3.2.3 Concentration drop in partially wetted membrane

A major challenge in membrane contactor operations is the penetration of the absorbent in the membrane pores which causes wetting of the membrane leading to a significant amount of concentration drop due to increase in mass transfer resistance [70,71]. Simulations of the normalized (C/C_{max}) radial concentration drop of CO_2 in the 10 %, 20 % and 50% wetted portion of the membrane are shown in Figure 10, for [emim][OAc]. C in the figure represents local CO_2 concentration inside the wetted portion of the membrane while C_{max} is the maximum interfacial CO_2 concentration. Concentration drop presented here is only in the wetted portion of the membrane at axial length of L/2. This huge drop of concentration in the wetted portion starts near the gas filled portion of membrane moving towards the shell boundary from where the absorbent is penetrated. A significant drop of CO_2 concentration in the wetted portion of the membrane can be observed. When the membrane is 50 % wetted, a concentration drop of 80 %, 75 % and 72 % can be observed for [emim][OAc]. The same behavior and pattern of concentration drop shown in Figure 10 was observed for [emim][$EtSO_4$] and [emim][$MeSO_4$], respectively (presented in supplementary file). However, at lower wetting ratios the drop in the concentration for [emim][OAc] was much higher when compared to other two ILs. In case of 10 % wetting a drop of 57 % was observed for [emim][OAc] while for [emim][$EtSO_4$] and [emim][$MeSO_4$] it was 34 % and 33 % respectively.

Figure 10

3.3 Parametric study

3.3.1 Effect of porosity and tortuosity of the hollow fiber membrane

Porosity (ε) is a key parameter for membrane absorption process, which directly affects the absorption process. Porosity plays an important role in the development of solute concentration profile, thus influencing the mass transfer process. High porosity can lead to high flux but also increases the chances of membrane wetting, thus a threshold value of porosity must be used [9,72]. Membrane tortuosity (τ) provides opposite effects than porosity. Increase in tortuosity usually increases the mass transfer resistance of the membrane. Tortuosity for this study was calculated from porosity using equation 32. The correlation is proposed by Mackie & Meares[73], which is known to be very successful for the estimation of tortuosity, verified by the Iversen et al.[74] for membranes manufactured by phase inversion technique.

$$\tau = \frac{(2-\varepsilon)^2}{\varepsilon} \quad (32)$$

The study in this section is focused on the effect of porosity and tortuosity on the concentration profile of the three ILs. Figures 11a and 11b show the effect of porosity and tortuosity on the gas side dimensionless concentration of CO_2 at the outlet of the tube for [emim][OAc] and [emim][$EtSO_4$]. Both

physical absorbents [emim][$EtSO_4$] and [emim][$MeSO_4$] (presented in supplementary file) show almost the same effect on concentration profiles for porosity and tortuosity. Initial increase in porosity and decrease in tortuosity affected the CO_2 concentration in the tube. Initial Change in porosity (0.2 to 0.4) and tortuosity (16.2 to 6.4) decreases the dimensionless CO_2 concentration at the outlet of the tube by 0.46, 0.42 and 0.41 for [emim][OAc], [emim][$EtSO_4$] and [emim][$MeSO_4$], respectively. Further change in these parameters has a small effect compared to the initial change. If we consider the IL [emim][OAc], the drop in the concentration was noted to be 0.18 and 0.02 for increasing the porosity value from 0.4 to 0.6 and 0.6 to 0.8, respectively.

Figure 11

3.3.2 Effect of flow rates

Gas and absorbent flowrates have opposite effects on the CO_2 absorption behavior. A smaller gas flow rate and higher absorbent flowrate increases the CO_2 removal efficiency[21,75]. The effect of gas and IL flow rates on CO_2 absorption was studied for nine different pairs of gas-IL flow rates. A decrease in gas flow rate increases residence time for mass transfer. An increase in IL flow rate provides efficient mass transfer due to increase in treated amount of absorbent and higher concentration gradient. Figure 12 shows dimensionless concentration of CO_2 in the tube side against axial length of the contractor. Both gas/IL flow rates were varied from 20 $ml.min^{-1}$ to 100 $ml.min^{-1}$. For all three ILs, 20/100 $ml.min^{-1}$ pair of gas/IL flow rate was most efficient. The gas/IL flowrate pair 100/20 $ml.min^{-1}$ was found to be the most inefficient. It can be noted that gas flow rate has higher effect on the absorption than IL flow rate. While keeping the gas flow rate at 20 $ml.min^{-1}$ and reducing the IL flow rate to 20 $ml.min^{-1}$ resulted in a very efficient absorption compared to higher gas flow rates. IL [emim][OAc], due to higher absorption capacity was able to withstand for gas flow rates higher than 100 $ml.min^{-1}$, while other physical absorbents were not able to absorb enough CO_2 at higher gas flowrates.

Figure 12

4 Conclusions

A 2-D comprehensive mathematical model for transport of CO_2 was developed for a hollow fiber membrane contactor operating in steady-state and pseudo steady-state modes. For pseudo steady-state mode, the model was further linked with a dynamic model of an absorbent tank where ILs used as extractant were recirculated. Developed models were validated with previous reported experimental results for [emim][OAc] and [emim][$EtSO_4$]; whereas the CO_2 absorption behavior was determined theoretically for the IL [emim][$MeSO_4$]. Coupled models predict the absorption of CO_2 in ILs, which is recirculated from the tank to the shell of the contactor. CO_2 solubility in the three ILs were studied in terms of Henry's law constant, which was calculated from experimental PTx data at VLE. Effect of temperature on CO_2 solubility and diffusivity were studied, which was further used to see the effect of temperature on CO_2 absorption in membrane contactor. Both axial and radial concentration profiles of CO_2 were systematically studied. Variations in overall mass transfer coefficient with time were

investigated. IL [emim][OAc] was observed to have more CO_2 absorption potential and can withstand for a longer time compared to other two ILs. IL [emim][$MeSO_4$] has shown more efficiency compared to [emim][$EtSO_4$]. Overall mass transfer coefficient decreases with high magnitude initially and after some time the decrease become gradual with time. Solubility and diffusivity of CO_2 in ILs had strong dependency on temperature. Increase in temperature resulted in higher diffusivity and lower solubility which diminished the CO_2 absorption in ILs. Wetted portion of the membrane showed a high magnitude drop in the concentration of CO_2. An increase in porosity and decrease in tortuosity reduced the mass transfer resistance in the membrane. Gas/IL flowrate pair of 20/100 ml.min^{-1} was found very efficient during parametric study. An experimental and modelling work on absorption and stripping of CO_2 in HFMCs coupled with other ILs is under study.

References

1. Atchariyawut, S., Jiraratananon, R. & Wang, R. Separation of CO2 from CH4 by using gas-liquid membrane contacting process. *J. Memb. Sci.* **304**, 163–172 (2007).

2. Atchariyawut, S., Feng, C., Wang, R., Jiraratananon, R. & Liang, D. T. Effect of membrane structure on mass-transfer in the membrane gas-liquid contacting process using microporous PVDF hollow fibers. *J. Memb. Sci.* **285**, 272–281 (2006).

3. Sreedhar, I., Nahar, T., Venugopal, A. & Srinivas, B. Carbon capture by absorption – Path covered and ahead. *Renew. Sustain. Energy Rev.* **76**, 1080–1107 (2017).

4. Metz, B. *Climate Change 2007: Mitigation. Contribution of Working Group III to the Fourth Assessment Report of the Intergovernmental Panel on Climate Change*. *Cambridge University Press Cambridge UK and New York NY Retrieved June* vol. 26 (2007).

5. Edmonds J. No Title. in *Proceedings of the 9th international conference on greenhouse gas control technologies.* (2008).

6. MacDowell, N. *et al.* An overview of CO2 capture technologies. *Energy Environ. Sci.* **3**, 1645 (2010).

7. Freund, P. Making deep reductions in CO2 emissions from coal-fired power plant using capture and storage of CO2. *Proc Inst Mech Eng Part A J Power Eng* **217**, 1–8 (2003).

8. Dai, Z., Noble, R. D., Gin, D. L., Zhang, X. & Deng, L. Combination of ionic liquids with membrane technology: A new approach for CO2separation. *J. Memb. Sci.* **497**, 1–20 (2016).

9. Zhao, S. *et al.* Status and progress of membrane contactors in post-combustion carbon capture: A state-of-the-art review of new developments. *J. Memb. Sci.* **511**, 180–206 (2016).

10. Rao, A. B. & Rubin, E. S. A Technical, Economic, and Environmental Assessment of Amine-Based CO 2 Capture Technology for Power Plant Greenhouse Gas Control. *Environ. Sci. Technol.* **36**, 4467–4475 (2002).

11. Li, B., Duan, Y., Luebke, D. & Morreale, B. Advances in CO2 capture technology: A patent review. *Appl. Energy* **102**, 1439–1447 (2013).

12. Lu, J. G. *et al.* CO2capture by membrane absorption coupling process: Application of ionic liquids. *Appl. Energy* **115**, 573–581 (2014).

13. Saidi, M. Mathematical modeling of CO2absorption into novel reactive DEAB solution in hollow fiber membrane contactors; kinetic and mass transfer investigation. *J. Memb. Sci.* **524**, 186–196 (2017).

14. Gebremariam, S. K. Modelling a Membrane Contactor for CO2 Capture. (2017).

15. Gabelman, A. & Hwang, S. Hollow ® ber membrane contactors. **159**, (1999).

16. Lu, J. G. *et al.* CO2capture by membrane absorption coupling process: Experiments and coupling process evaluation. *J. Memb. Sci.* **431**, 9–18 (2013).

17. Lv, Y. *et al.* Fabrication and characterization of superhydrophobic polypropylene hollow fiber membranes for carbon dioxide absorption. *Appl. Energy* **90**, 167–174 (2012).

18. Eslami, S., Mousavi, S. M., Danesh, S. & Banazadeh, H. Modeling and simulation of CO2 removal from power plant flue gas by PG solution in a hollow fiber membrane contactor. *Adv. Eng. Softw.* **42**, 612–620 (2011).

19. Lu, J. G., Zheng, Y. F., Cheng, M. D. & Wang, L. J. Effects of activators on mass-transfer enhancement in a hollow fiber contactor using activated alkanolamine solutions. *J. Memb. Sci.* **289**, 138–149 (2007).

20. Agrahari, G. K., Verma, N. & Bhattacharya, P. K. Application of hollow fiber membrane contactor for the removal of carbon dioxide from water under liquid-liquid extraction mode. *J. Memb. Sci.* **375**, 323–333 (2011).

21. Gong, Y., Wang, Z. & Wang, S. Experiments and simulation of CO2 removal by mixed amines in a hollow fiber membrane module. *Chem. Eng. Process. Process Intensif.* **45**, 652–660 (2006).

22. Paul, S., Ghoshal, A. K. & Mandal, B. Theoretical studies on separation of CO2by single and blended aqueous alkanolamine solvents in flat sheet membrane contactor (FSMC). *Chem. Eng. J.* **144**, 352–360 (2008).

23. Wang, R., Li, D. F. & Liang, D. T. Modeling of CO2 capture by three typical amine solutions in hollow fiber membrane contactors. *Chem. Eng. Process. Process Intensif.* **43**, 849–856 (2004).

24. Saeed, M. & Deng, L. Post-combustion CO2membrane absorption promoted by mimic enzyme. *J. Memb. Sci.* **499**, 36–46 (2016).

25. Yan, S., He, Q., Zhao, S., Wang, Y. & Ai, P. Biogas upgrading by CO2 removal with a highly selective natural amino acid salt in gas-liquid membrane contactor. *Chem. Eng. Process. Process Intensif.* **85**, 125–135 (2014).

26. Ramdin, M., De Loos, T. W. & Vlugt, T. J. H. State-of-the-art of CO \n 2 capture with ionic liquids. *Ind. Eng. Chem. Res.* **51**, 8149–8177 (2012).

27. Blanchard, L. a & Hancu, D. Green processing using ionic liquids and CO2. *Nature* **399**, 28–29 (1999).

28. Anthony, J. L., Maginn, E. J. & Brennecke, J. F. Solubilities and Thermodynamic Properties of Gases in the Ionic Liquid 1-n -Butyl-3-methylimidazolium Hexafluorophosphate. *J. Phys. Chem. B* **106**, 7315–7320 (2002).

29. Rogers, R. D. & Seddon, K. R. 2003_Seddon_Ionic_Liquids_Solvents_of_the_future.

30. Zhang, X. *et al.* Carbon capture with ionic liquids: overview and progress. *Energy Environ. Sci.* **5**, 6668 (2012).

31. Zhang, J. *et al.* Supported absorption of CO2 by tetrabutylphosphonium amino acid ionic liquids. *Chem. - A Eur. J.* **12**, 4021–4026 (2006).

32. Shannon, M. S. & Bara, J. E. Reactive and Reversible Ionic Liquids for CO 2 Capture and Acid Gas Removal. *Sep. Sci. Technol.* **47**, 178–188 (2012).

33. Luo, X. & Wang, C. The development of carbon capture by functionalized ionic liquids. *Curr. Opin. Green Sustain. Chem.* **3**, 33–38 (2017).

34. Mejía, I., Stanley, K., Canales, R. & Brennecke, J. F. On the high-pressure solubilities of carbon dioxide in several ionic liquids. *J. Chem. Eng. Data* **58**, 2642–2653 (2013).

35. Yokozeki, A., Shiflett Mark, B., Junk Christopher, P., Grieco Liane, M. & Foo, T. Physical and chemical absorptions of carbon dioxide in room-temperature ionic liquids. *J. Phys. Chem. B* **112**, 16654–16663 (2008).

36. Yim, J. H., Ha, S. J. & Lim, J. S. Measurement and Correlation of CO2Solubility in 1-Ethyl-3-methylimidazolium ([EMIM]) Cation-Based Ionic Liquids: [EMIM][Ac], [EMIM][Cl], and [EMIM][MeSO4]. *J. Chem. Eng. Data* **63**, 508–518 (2018).

37. Shiflett, M. B. & Yokozeki, A. Phase behavior of carbon dioxide in ionic liquids: [emim][acetate],

[emim][trifluoroacetate], and [emim][acetate] + [emim][trifluoroacetate] mixtures. *J. Chem. Eng. Data* **54**, 108–114 (2009).

38. Shiflett, M. B. *et al.* Phase Behavior of CO_2 in Room-Temperature Ionic Liquid 1-Ethyl-3-Ethylimidazolium Acetate. *ChemPhysChem* **13**, 1806–1817 (2012).

39. Luis, P., Garea, A. & Irabien, A. Zero solvent emission process for sulfur dioxide recovery using a membrane contactor and ionic liquids. *J. Memb. Sci.* **330**, 80–89 (2009).

40. Albo, J., Luis, P. & Irabien, A. Carbon Dioxide Capture from Flue Gases Using a Cross-Flow Membrane Contactor and the Ionic Liquid 1-Ethyl-3-methylimidazolium Ethylsulfate. *Ind. Eng. Chem. Res.* **49**, 11045–11051 (2010).

41. Albo, J. & Irabien, A. Non-dispersive absorption of CO 2 in parallel and cross-flow membrane modules using EMISE. *J. Chem. Technol. Biotechnol.* **87**, 1502–1507 (2012).

42. Gómez-Coma, L., Garea, A. & Irabien, A. Non-dispersive absorption of CO2in [emim][EtSO4] and [emim][Ac]: Temperature influence. *Sep. Purif. Technol.* **132**, 120–125 (2014).

43. Jie, X., Chau, J., Obuskovic, G. & Sirkar, K. K. Preliminary studies of CO2 removal from precombustion syngas through pressure swing membrane absorption process with ionic liquid as absorbent. *Ind. Eng. Chem. Res.* **52**, 8783–8799 (2013).

44. Chau, J., Obuskovic, G., Jie, X. & Sirkar, K. K. Pressure swing membrane absorption process for shifted syngas separation: Modeling vs. experiments for pure ionic liquid. *J. Memb. Sci.* **453**, 61–70 (2014).

45. Finotello, A., Bara, J. E., Camper, D. & Noble, R. D. Room-temperature ionic liquids: Temperature dependence of gas solubility selectivity. *Ind. Eng. Chem. Res.* **47**, 3453–3459 (2008).

46. Happel, J. Viscous flow relative to arrays of cylinders. *AIChE J.* **5**, 174–177 (1959).

47. Bird, R. B., Stewart, W. E. & Lightfoot, E. N. *Transport Phenomena*. *Transport Phenomena* (2002). doi:10.1016/j.ijhydene.2006.08.059.

48. Fuller, E. N., Schettler, P. D. & Giddings, J. C. A new method for prediction of binary gas-phase diffusion coefficients. *Ind. Eng. Chem.* **58**, 18–27 (1966).

49. Albo, J., Luis, P. & Irabien, A. Absorption of coal combustion fl ue gases in ionic liquids using different membrane contactors. *Desalin. Water Treat.* **27**, 54–49 (2011).

50. Dai, Z., Usman, M., Hillestad, M. & Deng, L. Modelling of a tubular membrane contactor for pre-combustion CO 2 capture using ionic liquids: Influence of the membrane configuration, absorbent properties and operation parameters. *Green Energy Environ.* **1**, 266–275 (2016).

51. Perry, S. *et al. Chemical Engineers ' Handbook Seventh*. *Society* vol. 27 (1997).

52. Jalili, A. H. *et al.* Solubility and diffusion of CO2and H2S in the ionic liquid 1-ethyl-3-methylimidazolium ethylsulfate. *J. Chem. Thermodyn.* **42**, 1298–1303 (2010).

53. Soriano, A. N., Doma, B. T. & Li, M. H. Carbon dioxide solubility in some ionic liquids at moderate pressures. *J. Taiwan Inst. Chem. Eng.* **40**, 387–393 (2009).

54. Wang, G. *et al.* Low viscosity triethylbutylammonium acetate as a task-specific ionic liquid for reversible CO2 absorption. *J. Chem. Eng. Data* **56**, 1125–1133 (2011).

55. Lei, Z., Dai, C. & Chen, B. Gas solubility in ionic liquids. *Chem. Rev.* **114**, 1289–1326 (2014).

56. Zubeir, L. F. *et al.* Solubility and Diffusivity of CO<inf>2</inf> in the Ionic Liquid 1-Butyl-3-methylimidazolium Tricyanomethanide within a Large Pressure Range (0.01 MPa to 10 MPa). *J. Chem. Eng. Data* **60**, 1544–1562 (2015).

57. Blath, J., Deubler, N., Hirth, T. & Schiestel, T. Chemisorption of carbon dioxide in imidazolium based ionic liquids with

carboxylic anions. *Chem. Eng. J.* **181–182**, 152–158 (2012).

58. Sander, R. Compilation of Henry's law constants (version 4.0) for water as solvent. *Atmos. Chem. Phys.* **15**, 4399–4981 (2015).

59. Nazet, A. *et al.* Densities, Viscosities, and Conductivities of the Imidazolium Ionic Liquids [Emim][Ac], [Emim][FAP], [Bmim][BETI], [Bmim][FSI], [Hmim][TFSI], and [Omim][TFSI]. *J. Chem. Eng. Data* **60**, 2400–2411 (2015).

60. Schmidt, H. *et al.* Experimental study of the density and viscosity of 1-ethyl-3- methylimidazolium ethyl sulfate. *J. Chem. Thermodyn.* **47**, 68–75 (2012).

61. Costa, A. J. L., Esperanca, M. S. S., Marrucho, I. M. & Rebelo, L. P. N. Densities and Viscosities of 1-Ethyl-3-methylimidazolium n -Alkyl Sulfates. *J. Chem. Eng. Data* **56**, 3433–3441 (2011).

62. Gómez, E., González, B., Calvar, N., Tojo, E. & Domínguez, Á. Physical Properties of Pure 1-Ethyl-3-methylimidazolium Ethylsulfate and Its Binary Mixtures with Ethanol and Water at Several Temperatures. *J. Chem. Eng. Data* **51**, 2096–2102 (2006).

63. Gómez-Coma, L., Garea, A. & Irabien, A. Mass Transfer Analysis of CO_2 Capture by PVDF Membrane Contactor and Ionic Liquid. *Chem. Eng. Technol.* **40**, 678–690 (2017).

64. Morgan, D., Ferguson, L. & Scovazzo, P. Diffusivities of gases in room-temperature ionic Liquids: Data and correlations obtained using a lag-time technique. *Ind. Eng. Chem. Res.* **44**, 4815–4823 (2005).

65. Moganty, S. S. & Baltus, R. E. Diffusivity of Carbon Dioxide in Room-Temperature Ionic Liquids. *Ind. Eng. Chem. Res.* **49**, 9370–9376 (2010).

66. Rebelo, L. P. N., Lopes, J. N. C., Esperança, J. M. S. S. & Filipe, E. On the critical temperature, normal boiling point, and vapor pressure of ionic liquids. *J. Phys. Chem. B* **109**, 6040–6043 (2005).

67. Araújo, J. M. M., Pereiro, A. B., Alves, F., Marrucho, I. M. & Rebelo, L. P. N. Nucleic acid bases in 1-alkyl-3-methylimidazolium acetate ionic liquids: A thermophysical and ionic conductivity analysis. *J. Chem. Thermodyn.* **57**, 1–8 (2013).

68. Ficke, L. E. THERMODYNAMIC PROPERTIES OF IMIDAZOLIUM AND PHOSPHONIUM BASED IONIC LIQUID MIXTURES WITH WATER OR CARBON DIOXIDE. (University of Notre Dame, 2010).

69. Okoturo, O. O. & VanderNoot, T. J. Temperature dependence of viscosity for room temperature ionic liquids. *J. Electroanal. Chem.* **568**, 167–181 (2004).

70. Wang, R., Zhang, H. Y., Feron, P. H. M. & Liang, D. T. Influence of membrane wetting on CO2 capture in microporous hollow fiber membrane contactors. *Sep. Purif. Technol.* **46**, 33–40 (2005).

71. Mosadegh-Sedghi, S., Rodrigue, D., Brisson, J. & Iliuta, M. C. Wetting phenomenon in membrane contactors - Causes and prevention. *Journal of Membrane Science* vol. 452 332–353 (2014).

72. Zhang, W. *et al.* Effect of porosity on mass transfer of gas absorption in a hollow fiber membrane contactor. *J. Memb. Sci.* **470**, 399–410 (2014).

73. Mackie, J. S. & Meares, P. The Diffusion of Electrolytes in a Cation-Exchange Resin Membrane. I. Theoretical. *Proc. R. Soc. A Math. Phys. Eng. Sci.* (1955) doi:10.1098/rspa.1955.0234.

74. Iversen, S. B., Bhatia, V. K., Dam-Johansen, K. & Jonsson, G. Characterization of microporous membranes for use in membrane contactors. *J. Memb. Sci.* **130**, 205–217 (1997).

75. Yan, S. ping *et al.* Experimental study on the separation of CO2from flue gas using hollow fiber membrane contactors without wetting. *Fuel Process. Technol.* **88**, 501–511 (2007).

76. Quijada-Maldonado, E., Van Der Boogaart, S., Lijbers, J. H., Meindersma, G. W. & De Haan, A. B. Experimental densities, dynamic viscosities and surface tensions of the ionic liquids series 1-ethyl-3-methylimidazolium acetate and

dicyanamide and their binary and ternary mixtures with water and ethanol at T = (298.15 to 343.15 K). *J. Chem. Thermodyn.* **51**, 51–58 (2012).

77. Requejo, P. F., González, E. J., Macedo, E. A. & Domínguez, Á. Effect of the temperature on the physical properties of the pure ionic liquid 1-ethyl-3-methylimidazolium methylsulfate and characterization of its binary mixtures with alcohols. *J. Chem. Thermodyn.* **74**, 193–200 (2014).

78. Almeida, H. F. D., Teles, A. R. R., Lopes-Da-Silva, J. A., Freire, M. G. & Coutinho, J. A. P. Influence of the anion on the surface tension of 1-ethyl-3- methylimidazolium-based ionic liquids. *J. Chem. Thermodyn.* **54**, 49–54 (2012).

79. Fröba, A. P., Kremer, H. & Leipertz, A. Density, Refractive Index, Interfacial Tension, and Viscosity of Ionic Liquids [EMIM][$EtSO_4$], [EMIM][NTf_2], [EMIM][$N(CN)_2$], and [OMA][NTf_2] in Dependence on Temperature at Atmospheric Pressure. *J. Phys. Chem. B* **112**, 12420–12430 (2008).

80. Rilo, E., Domínguez-Pérez, M., Vila, J., Varela, L. M. & Cabeza, O. Surface tension of four binary systems containing (1-ethyl-3-methyl imidazolium alkyl sulphate ionic liquid + water or + ethanol). *J. Chem. Thermodyn.* **49**, 165–171 (2012).

81. Santos, C. S. & Baldelli, S. Alkyl Chain Interaction at the Surface of Room Temperature Ionic Liquids: Systematic Variation of Alkyl Chain Length (R = C_1 −C_4 , C_8) in both Cation and Anion of [RMIM][$R - OSO_3$] by Sum Frequency G. *J. Phys. Chem. B* **113**, 923–933 (2009).

Tables:

Table 2. Specifications of the membrane module and operating conditions.

Parameter	Value	unit
Membrane material	Polypropylene	-
Inside radius of the tube (r_1)	1.1×10^{-4}	m
Outside radius of the tube (r_2)	1.5×10^{-4}	m
Membrane thickness (δ)	0.4×10^{-4}	m
Length of the contactor (L)	0.115	m
Number of fibers (n)	2300	-
Membrane pore diameter(d_p)	0.04	µm
Effective inner membrane area (A)	0.18	m^2
Porosity ($\boldsymbol{\varepsilon}$)	40	%
Packing factor	0.39	-
Tortuosity ($\boldsymbol{\tau}$)[a]	2.5	-
CO_2 amount in feed gas ($\boldsymbol{\varphi_v}$)	15	Vol %
Gas flow rate (Q_g)[b]	70	$ml.min^{-1}$
Liquid flow rate(Q_{lL})[c]	50	$ml.min^{-1}$

[a] Assumed as $\frac{(2-\varepsilon)^2}{\varepsilon}$

[b, c] Constant, unless mentioned

Table 2. Properties of the Ionic Liquids at 298 K

Property	Value	Purity	w (H_2O)	Reference
Viscosity: μ (mPa.s); 298 K				
[emim][OAc]	141.1	> 0.95 w/w	1.25×10^{-3}	59
	132.9	> 0.95 w/w	1.30×10^{-3}	76
[emim] [$EtSO_4$]	097.2	≥ 0.98 w/w	3.00×10^{-4}	60
	101.4	-	-	76
[emim][$MeSO_4$]	078.8	99 %	-	61
Density: ρ (g.cm-3); 298 K				
[emim][OAc]	1.099	> 0.95 w/w	1.25×10^{-3}	59
	1.097	> 0.95 w/w	1.30×10^{-3}	76
[emim] [$EtSO_4$]	1.237	≥ 0.98 w/w	3.00×10^{-4}	60
	1.240	-	-	76
[emim][$MeSO_4$]	1.282	> 99 %	-	61
	1.280	> 0.99 w/w	-	77
Surface Tension : ϒ (mN.m-1) ; 298 K				
[emim][OAc]	43.00	> 0.95 w/w	1.30×10^{-3}	76
	47.10	-	4.60×10^{-4}	78
[emim] [$EtSO_4$]	47.00	> 99 %	-	79
	47.13	-	2×10^{-4}	80
[emim][$MeSO_4$]	63.00	-	-	81

Table 3 Boundary conditions for model development

Boundary	Tube Side	Porous Membrane	Shell Side
$\boldsymbol{z = 0}$	$C_{CO_2-tube} = C_0$	No Flux	Convective flux
$\boldsymbol{z = L}$	Convective flux	No Flux	$C_{CO_2-shell} = 0\ (steady\ state)$; $C_{CO_2-tank}(t + \Delta t)\ (pseudo\ steady\ state)$
$\boldsymbol{r = 0}$	$\frac{\partial C_{CO_2-tube}}{\partial r} = 0$	-	-
$\boldsymbol{r = r_1}$	$C_{CO_2-tube} = C_{CO_2-membrane}$	$C_{CO_2-membrane} = C_{CO_2-tube}$	-
$\boldsymbol{r = r_2}$	-	$C_{CO_2-membrane} = \frac{C_{CO_2-shell}}{\acute{m}}$	$C_{CO_2-shell=}$ ḿ $C_{CO_2-membrane}$
$\boldsymbol{r = r_3}$	-	-	$\frac{\partial C_{CO_2-shell}}{\partial r} = 0$

Table 4 Transport parameters and mass transfer kinetics at 298 K

Parameter	Value	Reference
Reaction Kinetics: [emim][OAc]		
K_{eq}	220.3 ± 13.4	[35,38]
$\Delta\hat{H}$ (KJ.mol^{-1})	-30.81 ± 0.46	[35,38]
K_r (s^{-1})	2.7 x 10^{-3}	[63]
E (KJ.mol^{-1})	9.2	[63]
Henry's law constant: H (MPa), 298K		
[emim][OAc]	1.25	This work, Equation 10
[emim][$EtSO_4$]	11.70	This work, Equation 10
[emim][$MeSO_4$]	5.86	This work, Equation 10
Diffusivity of CO_2 in ILs: D_{CO_2} (cm^2. s^{-1}), 298K		
[emim][OAc]	2.64 x 10^{-06}	This work, Equation 19
[emim][$EtSO_4$]	3.38 x 10^{-06}	This work, Equation 19
[emim][$MeSO_4$]	3.88 x 10^{-06}	This work, Equation 19
Overall mass transfer coefficient: K_{ov} (m. s^{-1}), t=0		
[emim][OAc]	7.61 x 10^{-05}	This work, Equation 29
[emim][$EtSO_4$]	1.63 x 10^{-05}	This work, Equation 29
[emim][$MeSO_4$]	3.76 x 10^{-05}	This work, Equation 29

Table 5 Effect of temperature on radial concentration of CO_2 in the tube; Steady-state mode; $\boldsymbol{z = L/3}$ $\boldsymbol{Q_{IL} = 50\ ml.min^{-1}}$, $\boldsymbol{Q_g = 70\ ml.min^{-1}}$, $\boldsymbol{\varphi_v =\ 15}$ %,

Temperature (K)	**Radial concentration, C_{CO_2-tube}/C_0**		
	[emim][OAc]	[emim] [$EtSO_4$]	[emim][$MeSO_4$]
291	0.12	0.89	0.31
318	0.18	0.94	0.78
333	0.21	0.97	0.91

Figures:

Figure 1 Molecular structures of the cation (a) [emim]; and anions, (b) [OAc], (c) [$EtSO_4$], (d) [$MeSO_4$]

Figure 2 Schematic representation of setup assumed to be modeled

Figure 3 Schematic diagram of the section used for model development

Figure 4. Validation of simulations with experimental data (a) Simulations of [emim][OAc] with experimental data of [emim][OAc], (b) Simulations of [emim][$EtSO_4$] and [emim][$MeSO_4$] with experimental data of [emim][$EtSO_4$]; $\boldsymbol{Q_{IL} = 50\ ml.min^{-1}}$, $\boldsymbol{Q_g = 70\ ml.min^{-1}}$, $\boldsymbol{\varphi_v = 15\ \%}$

Figure 5 Dimensionless concentration profile of CO_2 in the tube for (a) [emim][OAc], (b)[emim][$EtSO_4$], (c)[emim][$MeSO_4$];$\boldsymbol{Q_{IL} = 50\ ml.min^{-1}}$, $\boldsymbol{Q_g = 70\ ml.min^{-1}}$, $\boldsymbol{\varphi_v = 15\ \%}$, $\boldsymbol{T = 318\ K}$ at various operating times.

Figure 6. Variation of K_{ov} with recirculation time estimated from modelling approach; $Q_{IL} = 50\ ml.min^{-1}$, $Q_g = 70\ ml.min^{-1}$, $\varphi_v = 15\ \%$, $T = 298\ K$.

Figure 7. Shell side (gas) concentration of CO_2 as a function of time estimated from modelling approach; $\mathbf{z = L/3}$, $\boldsymbol{Q_{IL} = 50\ ml.min^{-1}}$, $\boldsymbol{Q_g = 70\ ml.min^{-1}}$, $\boldsymbol{\varphi_v = 15\ \%}$, $\boldsymbol{T = 318\ K}$.

Figure 8 Effect of temperature on CO_2 diffusivity in ILs and Gas mixture

Figure 9 Effect of temperature on Henry's law constant of CO_2 in ILs

Figure 10. Radial concentration drop of CO_2 in wetted portion of membrane for [emim][OAc], estimated from modelling approach; Steady-state mode; $\boldsymbol{Q_{IL} = 50\ ml.min^{-1}}$, $\boldsymbol{Q_g = 70\ ml.min^{-1}}$, $\boldsymbol{\varphi_v = 15\ \%}$, $\boldsymbol{T = 318\ K}$.

Figure 11. Effect of porosity and tortuosity on radial concentration profile of CO_2 in the tube for (a) [emim][OAc], (b)[emim][$EtSO_4$], estimated from modelling approach. Steady-state mode; $\boldsymbol{Q_{IL} = 50\ ml.min^{-1}}$, $\boldsymbol{Q_g = 70\ ml.min^{-1}}$, $\boldsymbol{\varphi_v = 15\ \%}$, $\boldsymbol{T = 318\ K}$.

Figure 12. Effect of gas/IL flow rate on axial concentration profile of CO_2 in the tube for (a) [emim][OAc], (b)[emim][$EtSO_4$], (c)[emim][$MeSO_4$], estimated from modelling approach; Steady-state mode; $\boldsymbol{\varphi_v = 15\ \%}$, $\mathbf{T = 333\ K}$

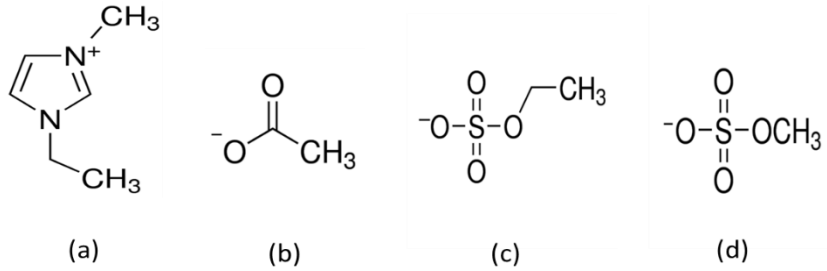

Figure 13. Molecular structures of the cation (a) [emim]; and anions, (b) [OAc], (c) [$EtSO_4$], (d) [$MeSO_4$]

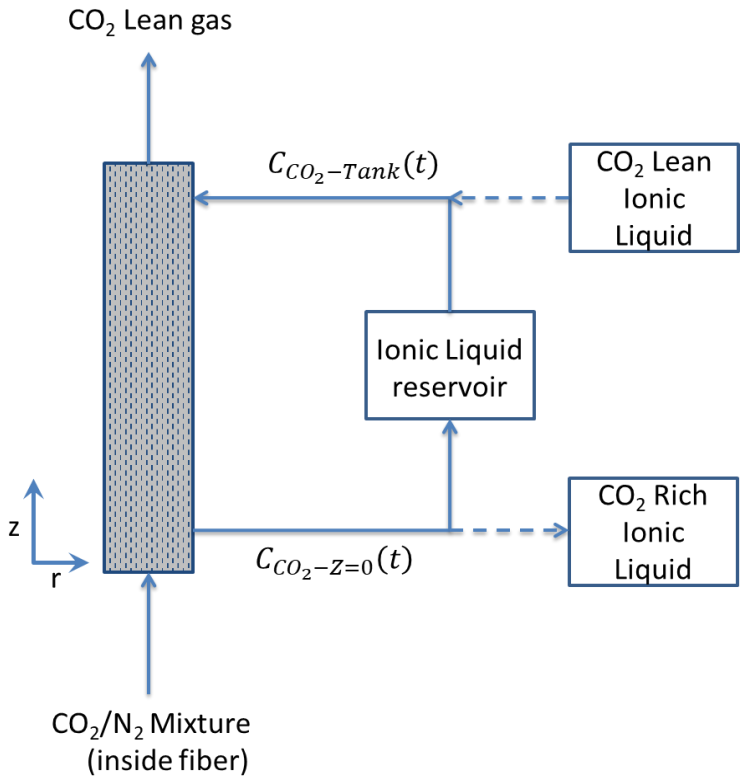

Figure 14. Schematic representation of setup assumed to be modeled

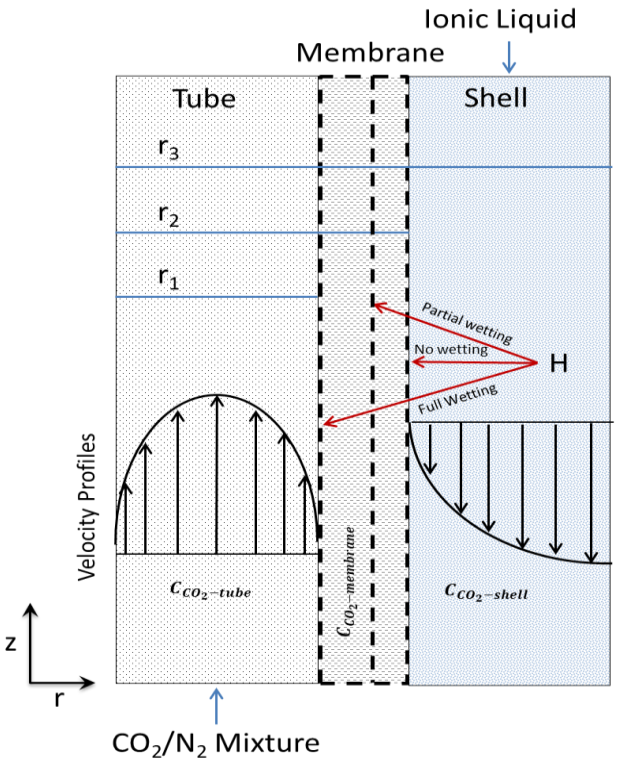

Figure 15. Schematic diagram of the section used for model development

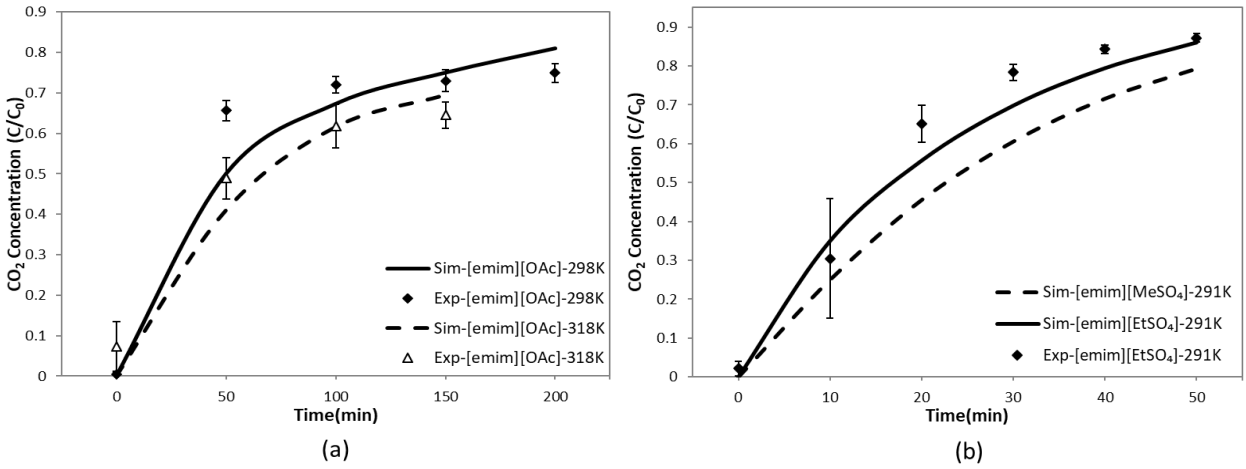

Figure 16. Validation of simulations with experimental data (a) Simulations of [emim][OAc] with experimental data of [emim][OAc], (b) Simulations of [emim][$EtSO_4$] and [emim][$MeSO_4$] with experimental data of [emim][$EtSO_4$]; $\boldsymbol{Q_{IL} = 50\ ml.min^{-1}}$, $\boldsymbol{Q_g = 70\ ml.min^{-1}}$, $\boldsymbol{\varphi_v =}$ **15** %

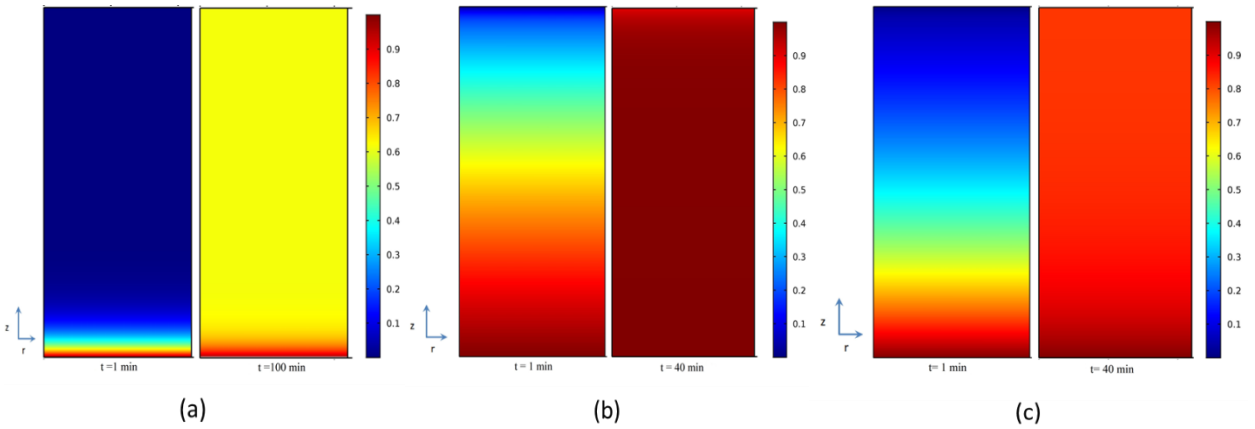

Figure 17. Dimensionless concentration profile of CO_2 in the tube for (a) [emim][OAc], (b)[emim][$EtSO_4$], (c)[emim][$MeSO_4$];$\boldsymbol{Q_{IL} = 50\ ml.min^{-1}}$, $\boldsymbol{Q_g = 70\ ml.min^{-1}}$, $\boldsymbol{\varphi_v = 15\ \%}$, $\boldsymbol{T = 318\ K}$ at various operating times.

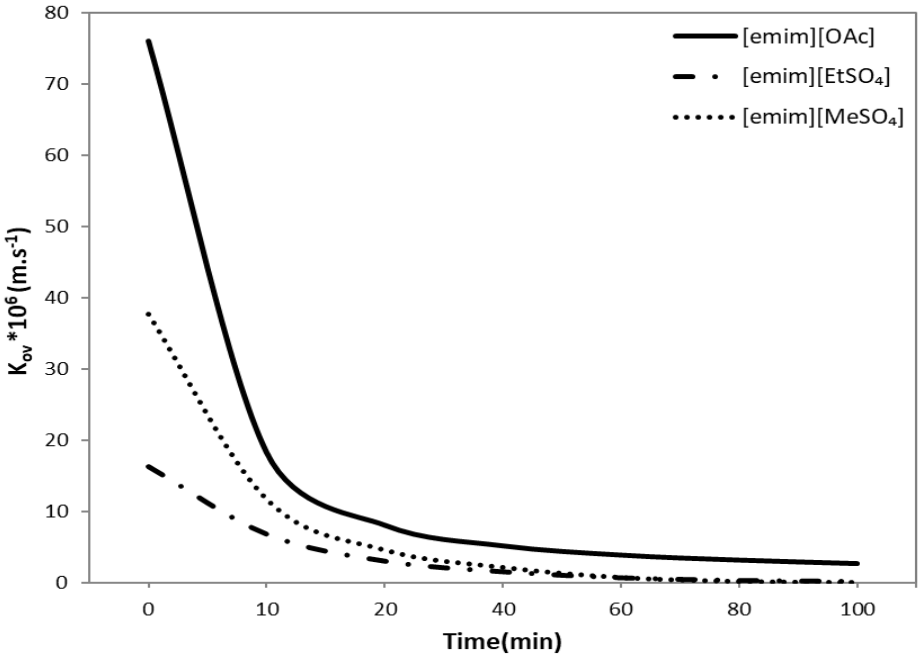

Figure 18. Variation of K_{ov} with recirculation time estimated from modelling approach; $\boldsymbol{Q_{IL} = 50\ ml.min^{-1}}$, $\boldsymbol{Q_g = 70\ ml.min^{-1}}$, $\boldsymbol{\varphi_v = 15\ \%}$, $\boldsymbol{T = 298\ K}$.

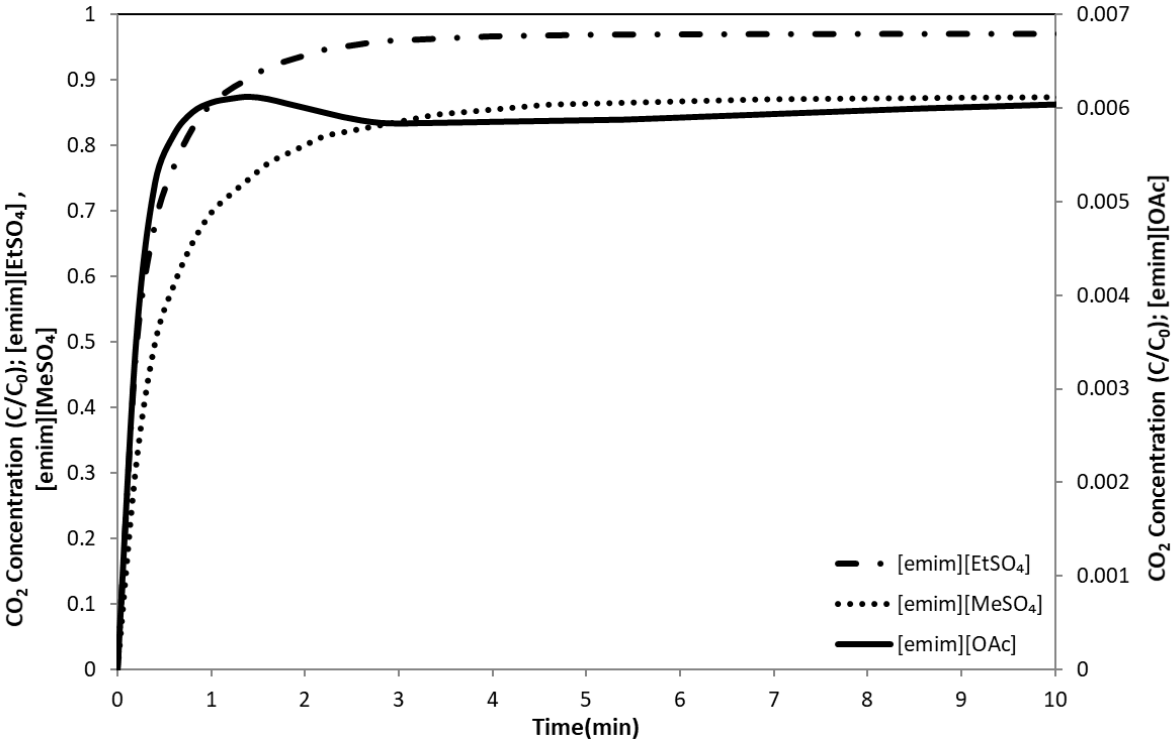

Figure 19. Shell side (gas) concentration of CO_2 as a function of time estimated from modelling approach; $\mathbf{z = L/3}$, $\boldsymbol{Q_{IL} = 50\ ml.min^{-1}}$, $\boldsymbol{Q_g = 70\ ml.min^{-1}}$, $\boldsymbol{\varphi_v =}$ **15** %, $\boldsymbol{T = 318\ K}$.

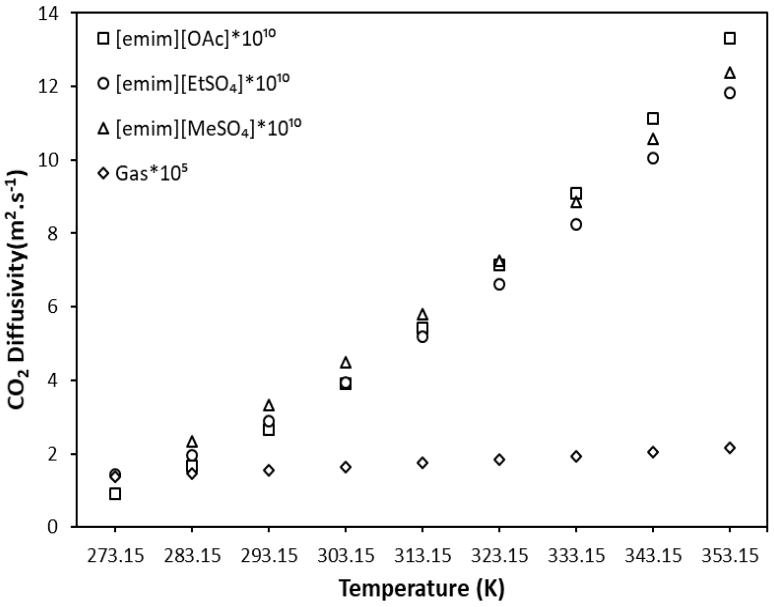

Figure 20. Effect of temperature on CO_2 diffusivity in ILs and gas mixture.

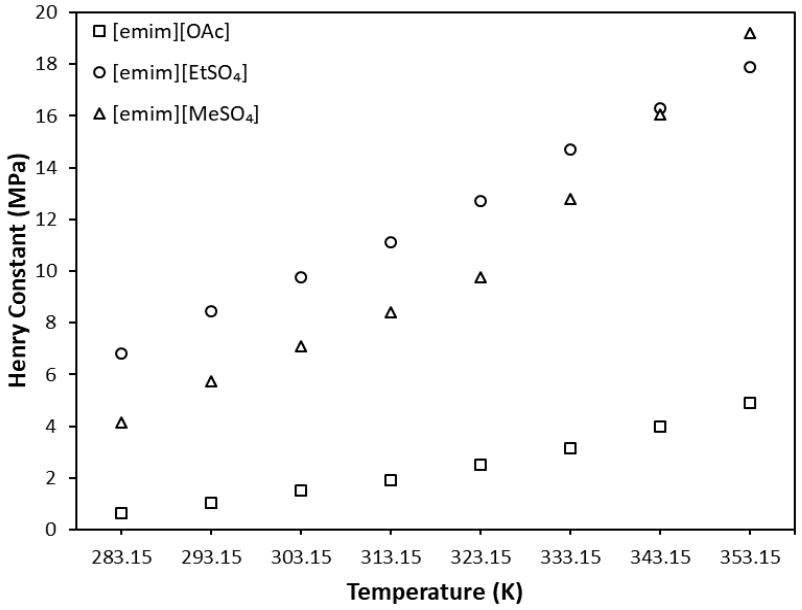

Figure 21. Effect of temperature on Henry's law constant of CO_2 in ILs.

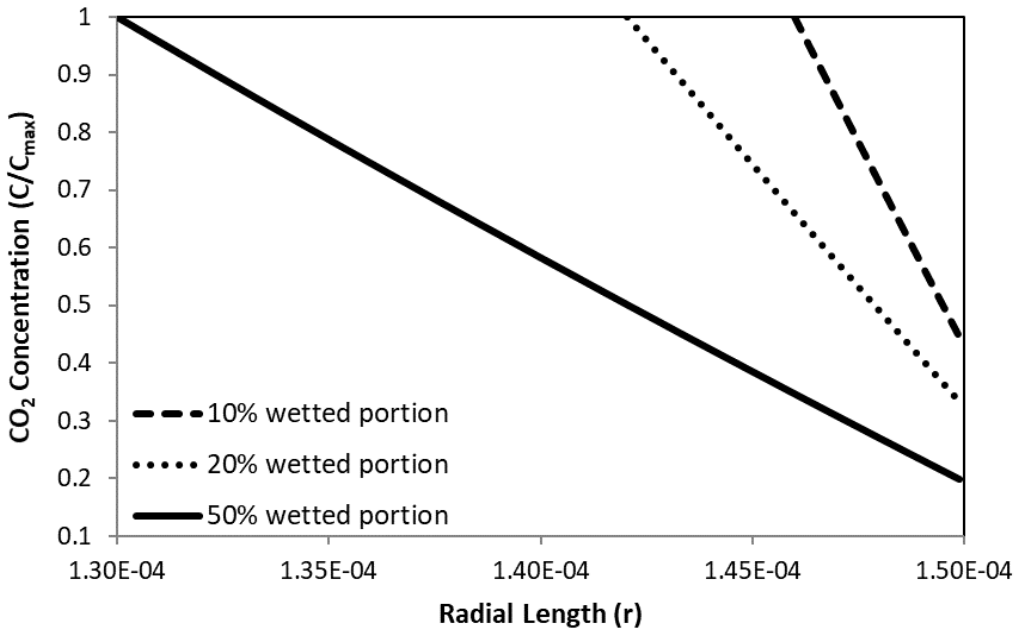

Figure 22. Radial concentration drop of CO_2 in wetted portion of membrane for [emim][OAc], estimated from modelling approach; Steady-state mode; $\boldsymbol{Q_{IL} = 50\ ml.min^{-1}}$, $\boldsymbol{Q_g = 70\ ml.min^{-1}}$, $\boldsymbol{\varphi_v = 15\ \%}$, $\boldsymbol{T = 318\ K}$,

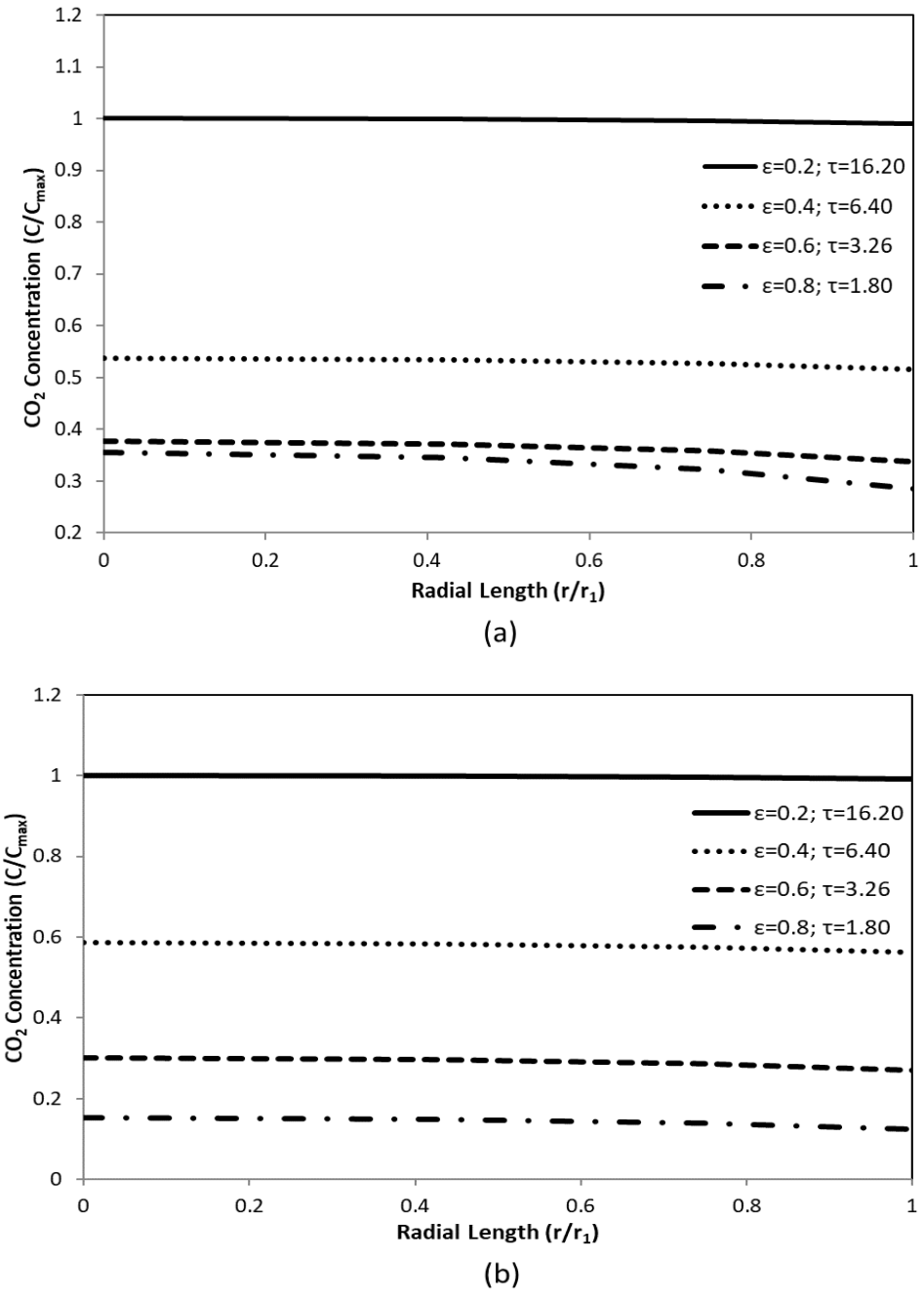

Figure 23. Effect of porosity and tortuosity on radial concentration profile of CO_2 in the tube for (a) [emim][OAc], (b)[emim][$EtSO_4$], estimated from modelling approach. Steady-state mode; $\boldsymbol{Q_{IL} = 50\ ml.min^{-1}}$, $\boldsymbol{Q_g = 70\ ml.min^{-1}}$, $\boldsymbol{\varphi_v = 15\ \%}$, $\boldsymbol{T = 318\ K}$.

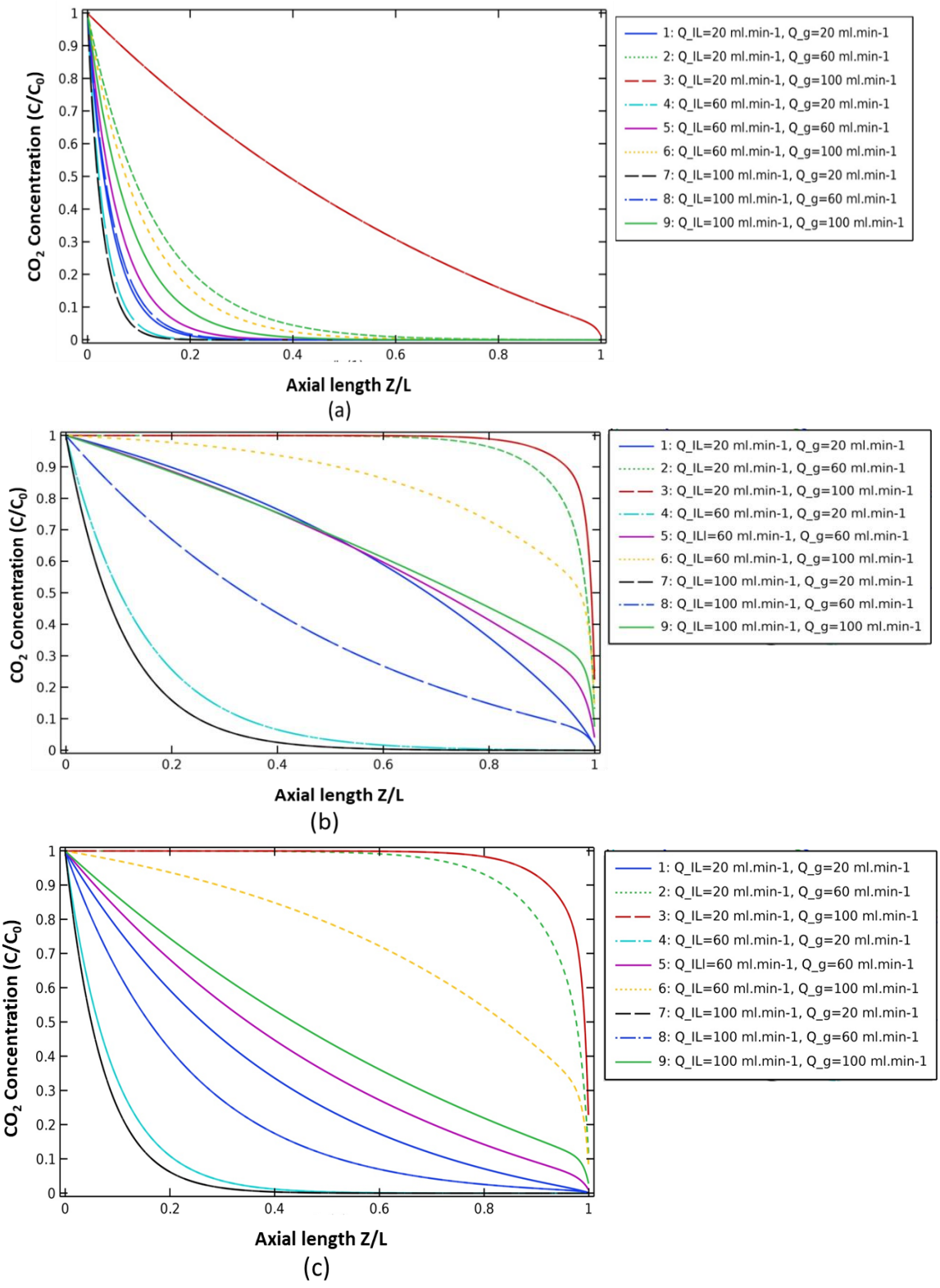

Figure 24. Effect of gas/IL flow rate on axial concentration profile of CO_2 in the tube for (a) [emim][OAc], (b)[emim][$EtSO_4$], (c)[emim][$MeSO_4$], estimated from modelling approach; Steady-state mode; $\boldsymbol{\varphi_v = 15\ \%, T = 333\ K}$